

Article

# Oblique Deposition of Ti/Pt/Au Electrode on Photonic Crystal for Vertical Current Injection <sup>†</sup>

Hanqiao Ye , Ryota Saeki, Yifan Xiong , Takashi Kogure, Masato Morifuji, Hirotake Kajii, Akihiro Maruta and Masahiko Kondow <sup>\*</sup> 

Graduate School of Engineering, Osaka University, 2-1 Yamada-oka, Suita, Osaka 565-0871, Japan;  
ye@e3.eei.eng.osaka-u.ac.jp (H.Y.); saeki@e3.eei.eng.osaka-u.ac.jp (R.S.); xiong@e3.eei.eng.osaka-u.ac.jp (Y.X.);  
kogure@e3.eei.eng.osaka-u.ac.jp (T.K.); morifuji@e3.eei.eng.osaka-u.ac.jp (M.M.);  
kajii@oled.eei.eng.osaka-u.ac.jp (H.K.); maruta@comm.eng.osaka-u.ac.jp (A.M.)

\* Correspondence: kondow@eei.eng.osaka-u.ac.jp; Tel.: +81-6-6879-7765

† Invited Paper.

Received: 16 October 2020; Accepted: 20 November 2020; Published: 25 November 2020



**Featured Application:** The technique described in this paper is meaningful for achieving the wavelength division multiplexing devices in intra-chip communications.

**Abstract:** We describe a device for inter-chip or intra-chip optical communications that contains the Circular Defect in photonic crystal (CirD) lasers array driven by vertical current injection. In order to improve the conductivity of the structure while also preventing current leakage, we introduce the oblique deposition of electrodes on a photonic crystal pattern by using an electron beam evaporation apparatus. The performance of an electrode is investigated by a transmission line method, and the CirD structure is fabricated with the electrode. We analyze the voltage-current relationship and confirm the CirD structure's low resistance of under  $1\text{ k}\Omega$ .

**Keywords:** optical communications; photonic crystal laser; electron beam evaporation

---

## 1. Introduction

As the amount of information circulating in the world increases rapidly, the traditional electronic circuits are beginning to show their shortcomings, such as the limits of transmission capacity, enormous energy consumption, and heat generation in data centers. Optical communication wavelength division multiplexing (WDM) devices are expected to replace electronic circuits for short-distance information transmission inside a chip or between chips [1,2]. The required bandwidth density is expected to be  $10\text{ Tbps/cm}^2$  for inter-chip communications [3] and  $10\text{ Pbps/cm}^2$  for intra-chip communications [4]. To obtain a higher capacity and smaller size, 2-D photonic crystal (PhC) lasers have attracted attention [5–8] because they have the capability of confining light in tiny resonators. As a prominent example, the lambda-scale embedded active-region photonic-crystal (LEAP) lasers showed a low threshold current of  $4.8\text{ }\mu\text{A}$  and an extremely low energy cost of  $4.4\text{ fJ/bit}$  under room-temperature (RT) continuous-wave (CW) conditions [9–13]. To obtain a 3-dB bandwidth of  $10\text{ GHz}$ , it was only necessary to inject a current of  $40\text{ }\mu\text{A}$  into the LEAP laser [11]. However, the electrodes of PhC laser diodes are generally located outside of the PhC pattern, and carriers diffuse laterally into the resonator in the PhC when the current is injected. Because the electrodes are large-sized, these designs make it difficult to further reduce the resistance and the footprint of laser diodes.

We previously proposed a laser diode with Circular Defect in PhC (CirD) [4,14–16]. In this device, 19 air holes in a hexagonal area were removed from the triangular PhC lattice, and 18 peripheral air holes were arranged in a ring shape. The whispering gallery mode (WGM) [16,17] was formed

along the periphery of the CirD cavity. By adjusting the radius of the CirD cavity, the resonant wavelength of the WGM can be modulated. A line-defect PhC waveguide is set beside the CirD cavities to propagate lasing light. The GaAs core layer (red part in Figure 1) is sandwiched by two AlGaAs/AlGaO<sub>x</sub> cladding layers, and they are covered by a GaAs contact layer. The cladding layers are selectively oxidized through air holes, and the AlGaAs at the cavity center is preserved as funnels for the current conduction because it is far from the outermost holes of the resonator. These cladding layers have such advantages as efficient vertical current injection, high thermal conductivity, and high mechanical stability, which together make RT-CW operations possible. Meanwhile, the oxidation width covers the WGM area perfectly, confining the light in the core layer so that the WGM can have a suitable quality factor  $Q$  around 5000–10,000.

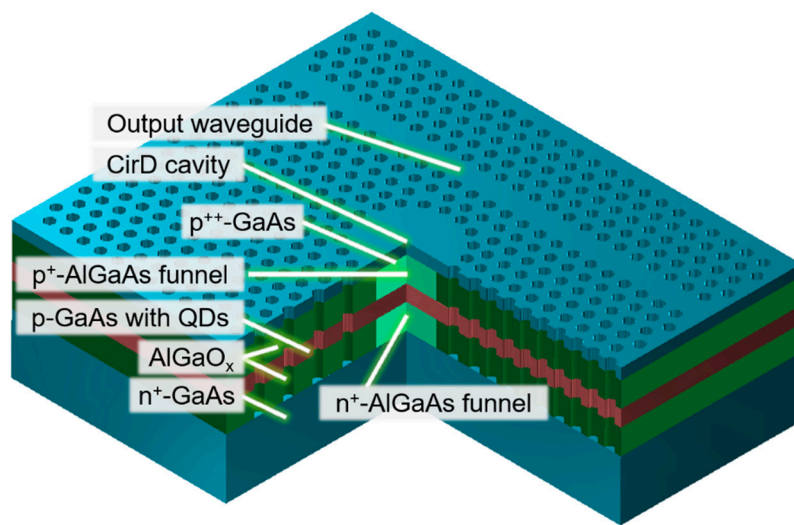


**Figure 1.** Schematic of a single Circular Defect (CirD) laser structure without electrodes.

Since the CirD lasers can be simply tuned to operate at different wavelengths by adjusting the cavity's radius, we designed a monolithic optical module containing a CirD laser array, which is suitable for WDM Application (Figure 2a) [4]. As a benefit from the small size of the CirD cavity, this WDM device has a very small footprint. Twenty CirD cavities with different lasing wavelengths are arranged on both sides of a single PhC line-defect waveguide. Since the lattice constant  $a$  of the triangular PhC lattice is approximately 360 nm, the distance between two adjacent cavities can be set to 5  $\mu\text{m}$ . Each cavity is surrounded by more than ten PhC lattice periods except for the direction to the waveguide, which provides sufficient horizontal light confinement. This laser array handling 20 wavelengths needs a length of only 100  $\mu\text{m}$ . Because the top GaAs contact layer allows the current to diffuse, all of the cavities must be electrically isolated for independent operations. Around each cavity, a current blocking trench (CBT) is made by selectively etching the GaAs contact layer on the AlGaO<sub>x</sub> cladding layer (Figure 2b) in order to obstruct the conductive path in the contact layer. The electrodes are deposited on each cavity. A 5- $\mu\text{m}$ -square area outside every cavity is used as the bonding pad, and thus the WDM device can be mounted to the circuits on the Si substrate by the flip-chip bonding method [4]. According to the rate equation calculations [4,7,17], a single CirD laser can be directly modulated at a rate of 50 Gbps under the injection current of 400  $\mu\text{A}$ , and thus a 20-channel CirD laser array can be expected to reach an extremely high bandwidth density of 10 Pbps/cm<sup>2</sup> [4].

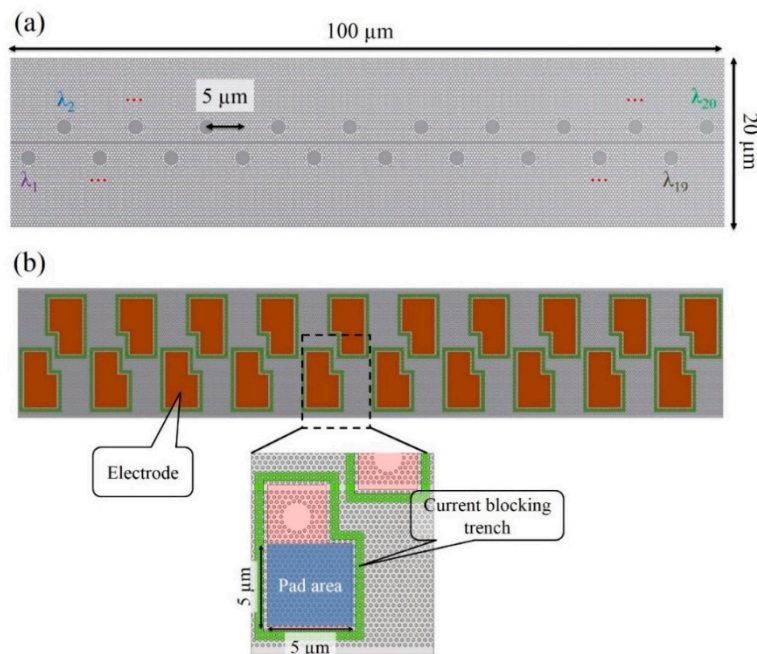


**Figure 2.** (a) Schematic of CirD laser array architecture enabling wavelength division multiplexing (WDM). (b) Schematic of CirD laser array in which each cavity is isolated by current blocking trench (CBT). A 5-μm-square area outside of cavity is used as the bonding pad. [4].

In our previous studies, the verticality of the profile of the 1.5-μm-deep air holes was improved to ensure the quality of the PhC structure [18,19]. Selective oxidation of AlGaAs was studied to obtain the ideal oxidization parameters for good light confinement [20]. To block the current between the different cavities, a selective etching process was also studied to fabricate the CBT on the PhC pattern [21]. However, the operation of a single CirD laser by vertical current injection has not been accomplished successfully, due to the immaturity of the technology for electrode fabrication on a PhC structure. First, current leakage is often found during the test, which is believed to be due to the electrode material contacting the core layer. Current leakage must be eliminated to ensure that the current is injected into the resonator. Furthermore, the resistance of a single diode must be reduced to a very low level so that the internal temperature does not rise excessively when sufficient current is injected. Current methods of electrode deposition are too inefficient to meet the above requirements. As far as we know, no report has demonstrated the ability to deposit thick electrodes for current injection on PhC. During the deposition, it is hard to prevent the electrode materials from covering the side faces of air holes in PhCs, which may cause current leakage and degradation of PhC optical properties. In the CirD device, the electrode should be tightly combined with the PhC surface to reduce the contact resistance. The resistance of a similar RT-CW photonic crystal laser diode is around 1 kΩ [11], so the total resistance of a single CirD laser should be under 1 kΩ, benefiting from the vertical current injection.

In this paper, we introduce the oblique deposition of electrodes to prevent metal materials from entering cladding layers or the core layer through the air holes of a PhC lattice. While the oblique deposition of metal for contacting nanostructured devices is an approach that has previously been utilized for the formation of contacts to optoelectronic devices containing arrays of semiconductor nanowires [22] or nanodots [23], this method has not been applied to 2-D photonic crystal with air holes before this study, as far as we know. We evaluate the specific contact resistance by the transmission line method. Here, we fabricate a single CirD cavity structure with a current blocking trench (CBT) outside the PhC pattern and deposit a Ti/Pt/Au electrode obliquely. Using this, the electrical characteristics are estimated to confirm that there is no leakage of current and the resistance of the structure is sufficiently low.

## 2. Process and Measurement System for Electrode Process Verification

Prior to the actual manufacture of the WDM device containing multiple CirD lasers, the conductive property of a single CirD diode structure must be verified to establish a reliable fabrication process. Therefore, in this study, we simplified the structure by placing the CBT outside of the PhC pattern with a CirD cavity, and dry etching was performed only one time. Different from the 5-μm-square bonding pad for the flip-bonding in the proposed device, a 90-μm-square electrode pad was designed for contact with the probe in the electrical measurement system. In the fabrication of the device in Figure 2, another selective etching must be performed for the CBT [21]. The CBT pattern would then be etched to the top of the upper AlGaO<sub>x</sub> layer to maintain the integrity of the waveguide. However, in this study, the dry etching process only needs to be carried out one time, making the process simpler. The epi-wafer used in this section was grown by molecular beam epitaxy (MBE). A 300-nm-thick n-GaAs buffer layer was grown on a 450-μm-thick n-GaAs substrate. The thickness of each of the two Al<sub>0.95</sub>Ga<sub>0.05</sub>As cladding layers is 500 nm. The GaAs core layer, including three stacked self-assembled InAs QD layers, has a total thickness of 220 nm. The photoluminescence (PL) peak of these QDs was designed at around 1290 nm (PL experimental data showed 1288.5 nm) to reduce the absorbing loss of output light (1300–1320 nm) propagating in the line defect waveguide. A 180-nm-thick p-GaAs contact layer is placed above the cladding layer. Figure 3 shows the fabrication process flow of the CirD Laser and its electrode for current injection measurement. First, the PhC structure was patterned on the resist (ZEP520A) by electron-beam (EB) lithography. An inductively coupled plasma reactive-ion etching (ICP-RIE) process was used to make the air holes and the CBT surrounding the PhC pattern (Figure 3b). This etching ends at the n-GaAs substrate layer.

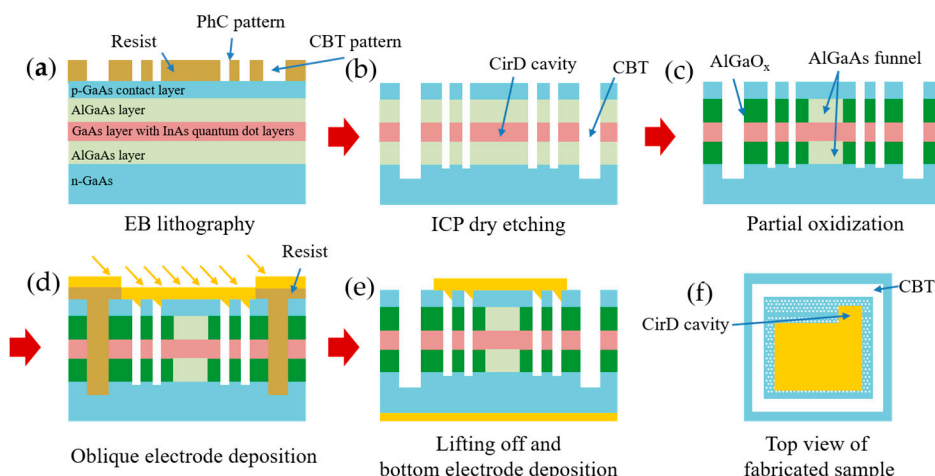


**Figure 3.** (a–e) Fabrication process of CirD laser and its electrode for current-voltage characteristics measurement. (f) Top view of the sample. The size of the electrode pad is 90  $\mu\text{m}$  square.

Then, the resist was removed using the ZDMAC remover. The AlGaAs layers were oxidized to AlGaO<sub>x</sub> through the air holes by H<sub>2</sub>O/N<sub>2</sub> steam at a temperature of 390 °C (Figure 3c). The process shown in Figure 3d is an oblique electrode deposition. We spin-coated the resist again and drew the electrode pattern. The resist enters the CBT, but this can be ignored. The resist in the CBT is removed in the step of lifting off. We deposited the electrode on the PhC pattern after performing another overlaid EB process. As a result, the electrode only remained inside the PhC pattern area surrounded by the CBT. The top electrode is made in the order of 30 nm of Ti, 10 nm of Pt, and 150 nm of Au. Then, we deposited the bottom electrode in the order of 20 nm of AuGe and 200 nm of Au by the resistive thermal evaporation method and annealed the sample to make the electrodes adhere tightly. With these processes, we can prevent the current from leaking outside of the PhC pattern. The only conductive path is in the unoxidized funnels. This is important for the independent operation of each

CirD cavity in the WDM device. In order to prevent metal atoms from entering the cladding layer or the core layer through the air holes, we considered depositing the Ti/Pt/Au metal atoms at an angle of  $60^\circ$  in the top electrode fabrication. EB evaporation is applied in making the top electrode so that the direction of material deposition can be controlled. As shown in Figure 4a, we use a holder to set the sample in the EB evaporation equipment (ULVAC, UEP-2000 OT-H/C) to make an  $\alpha = 60^\circ$  angle between the direction of the sample and the vapor flux. Due to the particle scattering in the deposition process [24], the direction of material deposition indicated by  $\beta$  is usually smaller than  $\alpha$ , so we predict that narrow channels could be formed on the air holes of the PhC lattice (Figure 4b).

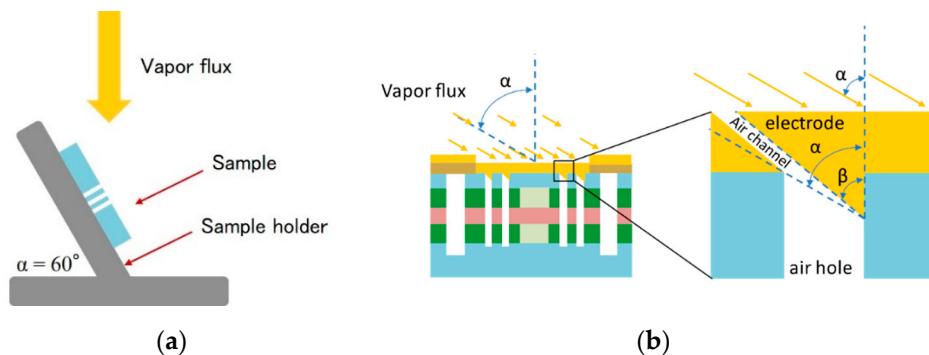


**Figure 4.** Schematic illustration of oblique electrode deposition. (a) A holder is used to make a  $60^\circ$  angle between the direction of the sample and the vapor flux. (b) Partial enlarged view of oblique electrode deposition principle.  $\alpha$  is the angle between the vapor flux and the substrate, and  $\beta$  is the direction of material deposition. When  $\alpha$  is set to  $60^\circ$ ,  $\beta$  is expected to be smaller than  $60^\circ$ .

### 3. Results and Discussion

#### 3.1. Analysis of the Results of Oblique Deposition

Figure 5 shows the results of the oblique electrode deposition. The left part of Figure 5a shows the electrode, and the right part is the bare PhC pattern. The lattice constant  $a$  is 360 nm and the radius of the air holes is 110 nm, which is approximately  $0.3a$ . Since we deposited the metal materials on non-flat samples with the PhC lattice, there are small holes in the electrode layer arranged just like the holes in the triangular PhC lattice pattern that can be seen in Figure 5a. By cleaving the sample and observing the cross section shown in Figure 5b, we observed that these holes were slanting channels connecting the PhC air holes with the outside, which is consistent with the prediction in Figure 4b. These channels are believed to be advantageous because they connect the inside and outside of the air holes in such a way that when the sample is stored in a vacuum environment, the air hole structures do not collapse due to uneven internal and external air pressures. As shown in Figure 5b, the electrode material was stacked into the contact layer at  $\beta \approx 53^\circ$ , a slightly smaller angle than  $\alpha = 60^\circ$ . No material enters the cladding layer or lower layers. This result indicates that the oblique electron beam deposition can perfectly prevent the metal material from entering the lower layers and influencing the optical properties of the PhC laser. We confirmed that there is no current leakage in the structure by estimating the voltage-current relationship.

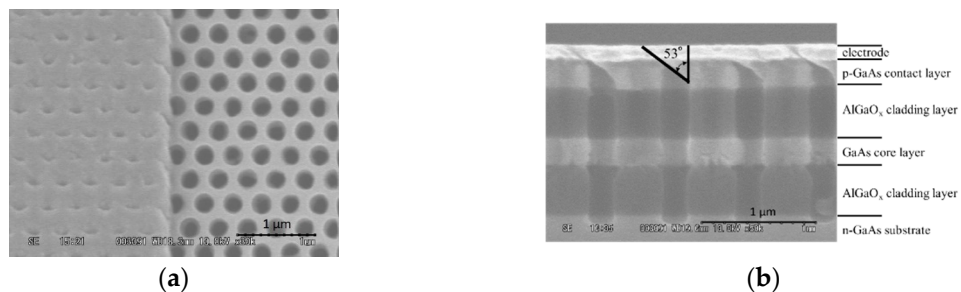


**Figure 5.** SEM images of top view (a) and cross-section view (b) of obliquely deposited electrode on the photonic crystal (PhC) structure.

### 3.2. Transmission Line Method (TLM) Measurement for Specific Contact Resistance

To achieve small resistance in the vertical current injection device, the resistance between the electrode and the GaAs contact layer with PhC holes needs to be small. Here, we used the transmission line method (TLM) for the resistance measurement [25].

Figure 6 shows the electrodes on a PhC pattern for the TLM measurement. We performed a similar process as that shown in Figure 3 to draw the PhC pattern without a cavity or waveguide and obliquely deposited the rectangular electrodes. We designed the CBT structure to prevent the current from flowing through outside. The specific contact resistance  $\rho_c$  is determined by characterizing the current-voltage relationship. Rectangular electrodes are used in the TLM measurement, which measures the distance-resistance relationship between rectangular electrodes, to obtain the contact resistance. In this study, the distances between the electrodes are  $d = 4, 6, 8 \dots 16 \mu\text{m}$  (Figure 6a), the electrode length is  $L = 50 \mu\text{m}$ , and the electrode width is  $w = 125 \mu\text{m}$ . By assuming that the semiconductor layer is equivalent to the transmission line, the resistance  $R_T$  existing between the electrodes can be easily expressed by [25]

$$R_T = 2R_c + \frac{R_{SH}d}{w}, \quad (1)$$

where  $R_{SH}$  is the sheet resistance of the semiconductor layer (GaAs) between the electrodes and  $R_c$  is the contact resistance defined by  $R_c = R_{SK}L_T/w$ .  $R_{SK}$  is the sheet resistance of the semiconductor layer just below the electrode, and  $L_T$  is called the propagation length. It can be assumed that the current flows in the area with length  $L_T$  in the electrode, which means that only the resistance of the area of width  $L_T$  in the electrode is included in the contact resistance. The propagation length  $L_T$  is defined by  $L_T = \sqrt{\rho_c/R_{SK}}$  (here,  $R_{SK} \approx R_{SH}$ ). Based on the above principles, the specific contact resistance  $\rho_c$  can be obtained from the slope of the approximate line of  $R_T$  and  $d$ . First, the contact resistance of the GaAs contact layer was measured without a photonic crystal structure for comparison. The  $\rho_c$  without PhC was  $6.4 \times 10^{-7} \Omega \cdot \text{cm}^2$  after annealing the sample at  $400^\circ\text{C}$  for 60 s. Then, we fabricated the sample with a PhC pattern and deposited the rectangular electrodes. Given the oblique direction shown by the arrows in Figure 6b, the stacked metal materials can be seen at the bottom of the electrode, not at the left or right side, which ensured accurate distances between the electrodes. Figure 7 shows the relationship between resistance and distance. Measurement results show that the specific contact resistance  $\rho_c$  was  $9.5 \times 10^{-7} \Omega \cdot \text{cm}^2$ , which is 1.5 times higher than that of the structure without a PhC pattern under the same annealing conditions. The resistance increases slightly, due to the decrease in the conductive area, which indicates that the bonding between the electrode and the contact layer is as tight as that in the no-PhC sample, and there is no current leakage through other layers. This result means that the structure fabricated by the oblique deposition has an acceptable electrical conductivity.

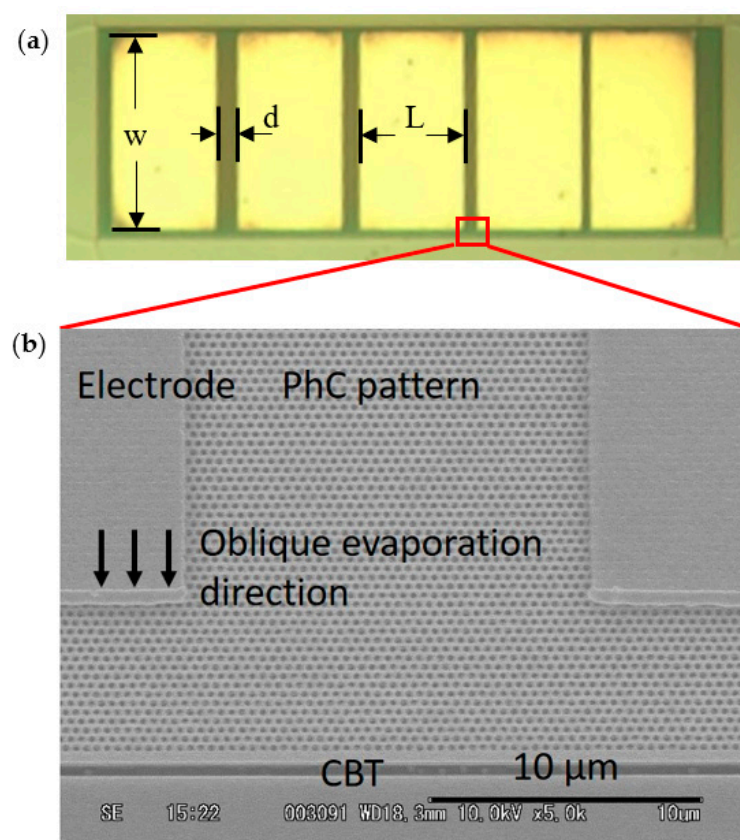


**Figure 6.** (a) Optical microscope image of the rectangular electrodes on PhC pattern for the transmission line method (TLM) measurement. Here,  $w = 125 \mu\text{m}$ ,  $L = 50 \mu\text{m}$ . (b) Partial SEM image of the electrodes for the TLM.

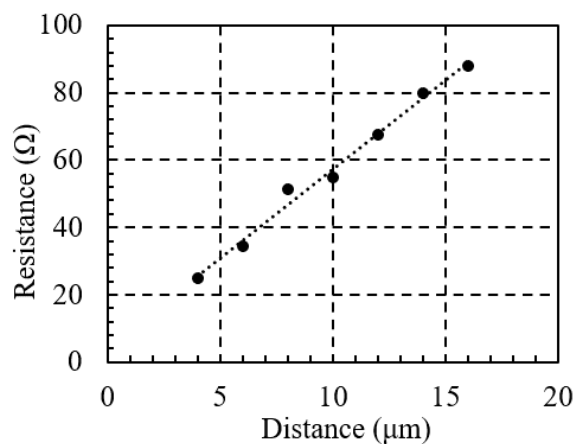


**Figure 7.** Relationship between resistance  $R_T$  and distance  $d$ .

### 3.3. Resistance Measurement for Vertical Current Injection

We manufactured a single CirD structure by the process shown in Figure 3, and we measured the current-voltage characteristics. During the measurement, the electrode pad shown in Figure 8a is touched by a probe connected with the anode of a voltage source (Keithley, 2400, Cleveland, OH, USA) and a multimeter (Hewlett Packard, 34401A, Palo Alto, CA, USA). The sample on molten indium was placed onto a copper plate, and the indium was cooled to fix the sample, making it easy to connect the bottom electrode with the cathodes of the voltage source. Figure 8b shows the current-voltage

relationship and the differential resistance of the sample analyzed from the voltages and currents. The differential resistance dropped below  $1\text{ k}\Omega$ , which is the target resistance for the CirD laser, when the current increased to  $300\text{ }\mu\text{A}$ . Since we assume the CirD laser works under the injection current of about  $400\text{ }\mu\text{A}$  to operate at  $50\text{ Gbps}$  [26], this conductive performance is acceptable.

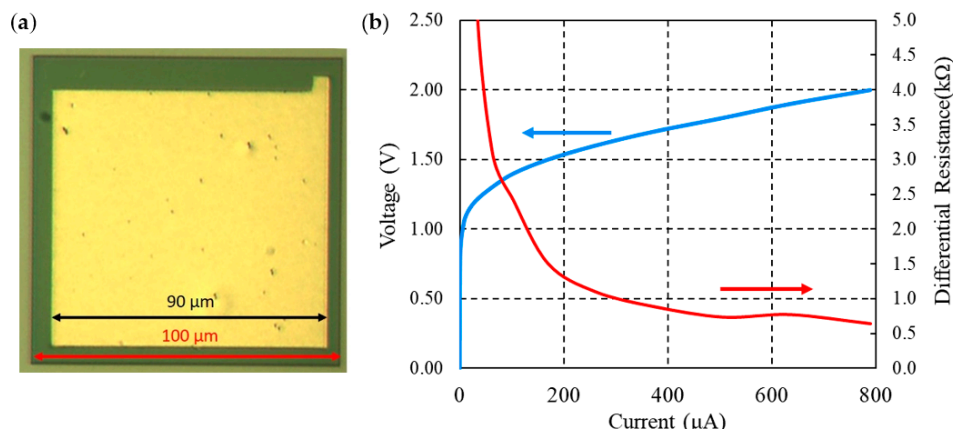


**Figure 8.** (a) Optical microscope image of single CirD structure with  $90\text{-}\mu\text{m}$ -square electrode pad in the  $100\text{-}\mu\text{m}$ -square PhC pattern. CirD cavity is in the upper-right corner. (b) Relationship of voltage between top and bottom electrodes with injection currents and relationship of differential resistance and currents.

#### 4. Conclusions

We described a device containing a CirD laser array for inter-chip or intra-chip WDM optical communications. By introducing oblique electrode deposition on a PhC pattern, we successfully prevented the electrode materials from entering below the contact layer through the air holes, ensuring that the current is injected into the funnels of the CirD cavity without leakage. We confirmed the conductive quality of the electrodes by the TLM and reduced the resistance of the CirD structure to below  $1\text{ k}\Omega$ . These results indicate that CirD lasers have great potential for future optical interconnects. With better cleaving technology and an appropriate optical measurement system, the next step of our study is to confirm the light-emitting characteristics of the CirD diode.

**Author Contributions:** Conceptualization is done by H.Y., Y.X., A.M., and M.K.; methodology is done by R.S., T.K., and A.M.; validation is done by Y.X., H.Y., T.K., and R.S.; investigation is done by R.S., H.Y., T.K., and Y.X.; data curation is done by H.Y. and R.S.; writing—original draft is done by H.Y.; writing—review and editing is done by H.Y., M.M., H.K., A.M., and M.K.; visualization is done by Y.X. and H.Y.; supervision is done by A.M. and M.K.; project administration is done by H.Y.; funding acquisition is done by M.M., H.K., A.M., and M.K. All authors have read and agree to the published version of the manuscript.

**Funding:** This work was partially supported by JSPS KAKENHI Grant JP19H02198, the Nanotechnology Platform of MEXT, Grant Number JPMXP09F20OS0006.

**Acknowledgments:** This work was partially supported by ULVAC, Inc., and Nippon Sheet Glass Foundation.

**Conflicts of Interest:** The authors declare no conflict of interest.

#### References

- Young, I.A.; Mohammed, E.; Liao, J.T.; Kern, A.M.; Palermo, S.; Block, B.A.; Reshotko, M.R.; Chang, P.L. Optical I/O technology for tera-scale computing. *IEEE J. Solid-State Circuits* **2010**, *45*, 235–248. [[CrossRef](#)]
- Miller, S.E. Integrated optics: An introduction. *Bell Syst. Tech. J.* **1969**, *48*, 2059–2069. [[CrossRef](#)]
- Arakawa, Y.; Nakamura, T.; Urino, Y.; Fujita, T. Silicon photonics for next generation system integration platform. *IEEE Commun. Mag.* **2013**, *51*, 72–77. [[CrossRef](#)]
- Xiong, Y.; Ye, H.; Umeda, T.; Mizoguchi, S.; Morifuji, M.; Kajii, H.; Maruta, A.; Kondow, M. Photonic Crystal Circular Defect (CirD) Laser. *Photonics* **2019**, *6*, 54. [[CrossRef](#)]

5. Yablonovitch, E. Inhibited spontaneous emission in solid-state physics and electronics. *Phys. Rev. Lett.* **1987**, *58*, 2059. [[CrossRef](#)] [[PubMed](#)]
6. Akahane, Y.; Asano, T.; Song, B.S.; Noda, S. High-Q photonic nanocavity in a two-dimensional photonic crystal. *Nature* **2003**, *425*, 944. [[CrossRef](#)] [[PubMed](#)]
7. Nomura, M.; Iwamoto, S.; Watanabe, K.; Kumagai, N.; Nakata, Y.; Ishida, S.; Arakawa, Y. Room temperature continuous-wave lasing in photonic crystal nanocavity. *Opt. Express* **2006**, *14*, 6308–6315. [[CrossRef](#)] [[PubMed](#)]
8. Nomura, M.; Kumagai, N.; Iwamoto, S.; Ota, Y.; Arakawa, Y. Photonic crystal nanocavity laser with a single quantum dot gain. *Opt. Express* **2009**, *17*, 15975–15982. [[CrossRef](#)] [[PubMed](#)]
9. Nozaki, K.; Baba, T. Carrier and photon analyses of photonic microlasers by two-dimensional rate equations. *IEEE J. Sel. Areas Commun.* **2005**, *23*, 1411–1417. [[CrossRef](#)]
10. Matsuo, S.; Shinya, A.; Kakitsuka, T.; Nozaki, K.; Segawa, T.; Sato, T.; Kawaguchi, Y.; Notomi, M. High-speed ultracompact buried heterostructure photonic-crystal laser with 13 fJ of energy consumed per bit transmitted. *Nat. Photonics* **2010**, *4*, 648–654. [[CrossRef](#)]
11. Takeda, K.; Sato, T.; Shinya, A.; Nozaki, K.; Kobayashi, W.; Taniyama, H.; Notomi, M.; Hasebe, K.; Kakitsuka, T.; Matsuo, S. Few-fJ/bit data transmissions using directly modulated lambda-scale embedded active region photonic-crystal lasers. *Nat. Photonics* **2013**, *7*, 569–575. [[CrossRef](#)]
12. Kuramochi, E.; Nozaki, K.; Shinya, A.; Takeda, K.; Sato, T.; Matsuo, S.; Taniyama, H.; Sumikura, H.; Notomi, M. Large-scale integration of wavelength-addressable all-optical memories on a photonic crystal chip. *Nat. Photonics* **2014**, *8*, 474. [[CrossRef](#)]
13. Matsuo, S.; Takeda, K.  $\lambda$ -Scale Embedded Active Region Photonic Crystal (LEAP) Lasers for Optical Interconnects. *Photonics* **2019**, *6*, 82. [[CrossRef](#)]
14. Morifuji, M.; Nakaya, Y.; Mitamura, T.; Kondow, M. Novel design of current driven photonic crystal laser diode. *IEEE Photonics Technol. Lett.* **2009**, *21*, 513–515. [[CrossRef](#)]
15. Xiong, Y.; Umeda, T.; Zhang, X.; Morifuji, M.; Kajii, H.; Maruta, A.; Kondow, M. Photonic crystal circular-defect microcavity laser designed for wavelength division multiplexing. *IEEE J. Sel. Top. Quantum Electron.* **2018**, *24*, 1–7. [[CrossRef](#)]
16. Miyamoto, Y.; Xiong, Y.; Okada, T.; Morifuji, M.; Kajii, H.; Kondow, M. Optical coupling characteristics between a circular defect resonator and a waveguide in a two-dimensional photonic crystal slab. *Photonics Nanostruct-Fundam Appl.* **2018**, *31*, 168–172. [[CrossRef](#)]
17. McCall, S.L.; Levi, A.F.J.; Slusher, R.E.; Pearton, S.J.; Logan, R.A. Whispering-gallery mode microdisk lasers. *Appl. Phys. Lett.* **1992**, *60*, 289–291. [[CrossRef](#)]
18. Kitabayashi, Y.; Mochizuki, M.; Ishikawa, F.; Kondow, M. Over 1.5  $\mu\text{m}$  Deep Dry Etching of Al-Rich AlGaAs for Photonic Crystal Fabrication. *Jpn. J. Appl. Phys.* **2013**, *52*, 04CG07. [[CrossRef](#)]
19. Zhang, X.; Takeuchi, K.; Cong, X.; Xiong, Y.; Morifuji, M.; Maruta, A.; Kajii, H.; Kondow, M. Dry etching of deep air holes in GaAs/AlGaAs-based epi-wafer having InAs quantum dots for fabrication of photonic crystal laser. *Jpn. J. Appl. Phys.* **2017**, *56*, 126501. [[CrossRef](#)]
20. Kondow, M.; Kawano, T.; Momose, H. Selective Oxidation of AlGaAs for Photonic Crystal Laser. *Jpn. J. Appl. Phys.* **2009**, *48*, 050202. [[CrossRef](#)]
21. Xiong, Y.; Tani, Y.; Cong, X.; Morifuji, M.; Kajii, H.; Maruta, A.; Kondow, M. Selective dry etching of GaAs/AlO<sub>x</sub> for realizing electrical isolation on monolithic integrated photonic crystal laser array. *Jpn. J. Appl. Phys.* **2020**, *59*, 086505. [[CrossRef](#)]
22. Senanayake, P.; Hung, C.H.; Shapiro, J.; Lin, A.; Liang, B.; Williams, B.S.; Huffaker, D.L. Surface plasmon-enhanced nanopillar photodetectors. *Nano Lett.* **2011**, *11*, 5279–5283. [[CrossRef](#)] [[PubMed](#)]
23. Schlykow, V.; Manganelli, C.L.; Römer, F.; Clausen, C.J.; Augel, L.; Schulze, J.; Katzer, J.; Schubert, M.A.; Witzigmann, B.; Schroeder, T.; et al. Ge (Sn) nano-island photodetectors with plasmonic antennas. *Nanotechnology* **2020**, *31*, 345203. [[CrossRef](#)] [[PubMed](#)]
24. Abelmann, L.; Lodder, C. Oblique evaporation and surface diffusion. *Thin Solid Film.* **1997**, *305*, 1–21. [[CrossRef](#)]
25. Schroder, D.K. Contact resistance, Schottky barriers and Electromigration. *Semicond. Mater. Device Charact.* **1998**, *2*, 133–199.

26. Ye, H.; Nishimura, T.; Xiong, Y.; Yamaguchi, T.; Morifuji, M.; Kajii, H.; Maruta, A.; Kondow, M. Analysis on high speed operation for photonic crystal circular defect laser. In Proceedings of the IEICE Society Conference 2019, Osaka, Japan, 10–13 September 2019; p. C-3-63.

**Publisher's Note:** MDPI stays neutral with regard to jurisdictional claims in published maps and institutional affiliations.



© 2020 by the authors. Licensee MDPI, Basel, Switzerland. This article is an open access article distributed under the terms and conditions of the Creative Commons Attribution (CC BY) license (<http://creativecommons.org/licenses/by/4.0/>).